



# Hydro-meteorological reconstruction and geomorphological impact assessment of the October, 2018 catastrophic flash flood at Sant Llorenç, Mallorca (Spain)

5 Jorge Lorenzo-Lacruz<sup>1</sup>, Celso Garcia<sup>1</sup>, Enrique Morán-Tejeda<sup>1</sup>, Arnau Amengual<sup>2</sup>, Víctor Homar<sup>2</sup>, Aina Maimó-Far<sup>2</sup>, Alejandro Hermoso<sup>2</sup>, Climent Ramis<sup>2</sup>, Romualdo Romero<sup>2</sup>

<sup>1</sup>Department of Geography, University of the Balearic Islands, Palma, 07122, Spain

<sup>2</sup>Department of Physics, University of the Balearic Islands, Palma, 07122, Spain

Correspondence to: Jorge Lorenzo-Lacruz ([j.lorenzo@uib.es](mailto:j.lorenzo@uib.es))

10

**Abstract.** An extraordinary convective rainfall event, unforeseen by most prediction models, generated a devastating flash flood in Sant Llorenç des Cardassar, Mallorca on October 9, 2018. Four people died in the town (13 people died in the entire affected area). The event was reconstructed, implementing an integrated flash flood modelling approach in this small (23.4 km<sup>2</sup>) and semi-arid ungauged Mediterranean catchment, with a highly nonlinear hydrological response to heavy precipitation, based on three components: (i) generation of radar-derived precipitation estimates during the event; (ii) modelling of an accurate discharge hydrograph yielded by the basin; and (iii) hydraulic simulation of the event and mapping of affected areas. Radar-derived rainfall estimates showed very high agreement with rain gauge data ( $R^2 = 0.98$ ). Modelled flooding extent is in close agreement with the observed extension by Copernicus Emergency Management Service, based on Sentinel-1 imagery, and both far exceed the extension for a 500-year return period flood. Hydraulic simulation showed that water reached a depth of 3 m at some points, and modelled water depths highly correlate ( $R^2 = 0.91$ ) with *in-situ* after-event measurements. The flash flood eroded and transported woody and abundant sediment debris, changing channel geomorphology. Water velocity greatly increased at bridge locations crossing the river channel, especially at those closer to Sant Llorenç town centre. This study shows how the very low predictability of this type of extreme convective rainfall events and the very short hydrological response times typical of small Mediterranean catchments continue to challenge the implementation of early warning systems, which effectively reduce people's exposure to flash flood risk in the region.

15  
20  
25

## 1. Introduction

The European Union member states reported 3,198 floods occurred between 1980-2015 (EU Floods Directive 2007/60/EC) (<http://rod.eionet.europa.eu/obligations/601>; <https://www.eea.europa.eu/data-and-maps/data/european-past-floods>). These



- 30 floods were responsible for 4,806 fatalities and an approximate total damage cost of 115,113 million euros. Spain reported more than 20 floods per 10,000 km<sup>2</sup>, one of the highest in Europe, with 652 fatalities (European Environment Agency, 2016). In 2018, flash floods killed 152 people across Europe, parts of northern Africa and the Middle East. The deadliest flash floods occurred in the Mediterranean area, including 5 events with 70 fatalities, concentrated in almost one month: October 9 to November 9 (European Severe Weather Database; <https://www.eswd.eu/>).
- 35 High-intensity precipitation episodes with a convective origin that fall over small catchment headwaters, generating a fast hydrological response characterised by a sudden flow event with steep rising and falling limbs and short lag times are known as flash floods (i.e., Borga et al., 2014; Marchi et al., 2010). In the western Mediterranean region, flash floods occur mostly in the autumn (Llasat et al., 2010) and generally they are more intense than in continental areas (Gaume et al., 2009). The relatively high sea surface temperature increases the available potential convective energy of the overlying moist air masses
- 40 through sensible and latent heat flux exchanges. Together with the intrusion of cold polar air masses aloft, the complex orography and acute land-sea contrasts promote, in many cases but not all, the lifting of low-level unstable air, favouring the triggering of deep moist convection. High precipitation rates can remain during several hours over individual catchments. This persistence is often associated with prominent orography or quasi-stationary convergence lines that anchor convection (Kolios and Feidas, 2010; Amengual et al., 2015). In the Spanish Mediterranean semi-arid region, many small- to medium-sized
- 45 catchments are steep and highly modified, and flood-prone areas are densely occupied. Many of these rivers are ephemeral, with short hydrological response times, and they are dominated by extreme events of low frequency and high magnitude. All these hydrological characteristics make flash flood forecasting and warning a big challenge for flood risk management (Marchi et al., 2010) and, more specifically, create challenges for flood risk perception, awareness and communication strategy (i.e., Bodoque et al., 2019)
- 50 This paper presents (forensic) reconstruction of the catastrophic flash flood that occurred on October 9, 2018 in the ephemeral river of Ses Planes, which crosses the town of Sant Llorenç des Cardassar, located east of the island of Mallorca (Fig. 1). An extreme rainstorm triggered a large magnitude flash flood that eroded and transported woody debris and sediment from the headwaters and along the fluvial valley, killing 13 people (4 in the town of Sant Llorenç) and damaging more than 300 dwellings, 30 stores and 324 vehicles (<https://sinobas.aemet.es/index.php?pag=detal&rep=1221>). The study relies on three
- 55 modelling components: (i) generation of radar-derived precipitation for the study area during the event; (ii) modelling of an accurate discharge hydrograph yielded by the catchment; and (iii) hydraulic simulation of the flash flood and mapping of affected areas, including flooding extent and timing, water depth and water velocity. Also presented are some of the geomorphological effects on the main channel, using very high-resolution orthophotographs and digital elevations models for comparison of pre- and post-flooding conditions.
- 60 This deadly flash flood had an important social impact on the region, the Balearic Islands, and in the country (the urban flooded area was already included in the Spanish national flood risk maps portal). Meteorology-based prediction methods failed at reproducing the convective clusters responsible for the intense rainfall episode over the area. Consequently, the Spanish meteorological agency (AEMET) shifted from orange to red alert for intensive rainfall only when the flood peak was nearly



upon the town. This extreme flood event has shaken the foundations of flood risk perception for the people of the Balearic  
65 Islands. How to face this challenge for hydro-meteorological modellers and forecasters, civil protection managers and policy  
makers is discussed in this paper.

## 2. Case study

### 2.1 Catchment description

70 The Ses Planes torrent is a small ephemeral stream located on the eastern part of the island of Mallorca (Fig. 1). The catchment  
has a drainage area of 23.4 km<sup>2</sup> at the entrance to the town of Sant Llorenç des Cardassar (8405 inhabitants). It is located in  
the Llevant Ranges, a Neogene horst structure composed mainly of carbonate deposits that have an Alpine internal  
compressional structure (Sabat et al., 1988). The topographic relief and the steepness of the slopes are important; over a few  
kilometres, the elevation increases from less than 100 m to small mountains of 400 m. The catchment has a well-developed  
75 drainage network, with a circular (fan) shape on the headwaters and an elongated *bottleneck* shape before the entrance of the  
town (Fig. 1). Forested areas are reduced and vegetation density is generally low, due to the prominence of sclerophyllous  
vegetation and rainfed crops, conditioned by thin soils. The Sant Llorenç catchment exhibits fast hydrological responses to  
heavy precipitation, resulting in fast Hortonian flows during intense rainfall episodes. However, high infiltration rates are also  
present because of the persistence of low soil moisture content and the existence of underlying karstic and dolomitic fractured  
80 bedrock that promotes deep percolation. Therefore, this catchment features a highly nonlinear hydrological response to heavy  
precipitation and large rainfall amounts.

The Ses Planes torrent has been affected by several severe flood events over the last half century: 12/10/1973, 3/09/1982,  
25/10/1985 and 06/09/1989 (Grimalt and Rodríguez-Perea, 1989). The latter was especially important; 156 mm of precipitation  
recorded in two hours generated a flash flood that affected some areas of the town and led local authorities to undertake the  
85 artificial channelization of the Ses Planes torrent where it crosses the Sant Llorenç urban area. In this study, an integrated flash  
flood modelling and mapping approach was implemented to reconstruct the flash flood event in this small ungauged  
Mediterranean catchment.

Although there are neither precipitation nor gauging stations within the Sant Llorenç watershed limits, the region is monitored  
by a Doppler C-band weather radar of the Spanish Agency of Meteorology (AEMET) network located 50 km away from the  
90 catchment. Within this region, raw precipitation is recorded by four automatic rain-gauge stations with a temporal resolution  
of 10 minutes. Daily rainfall amounts are also recorded in 17 additional rain gauges, all of them outside the Sant Llorenç  
watershed limits (Fig. 3a).



## 2.2 Synoptic situation

The large-scale meteorological pattern responsible for the deadly flash flood event was very well defined, according to the circulation systems seen at 500 hPa and at surface on that day (Fig. 2a). The 500 hPa analysis shows a deep trough that covered the North Atlantic, with a strong gradient of geopotential height at mid-latitudes that induced a strong south-westerly flow towards western and northern Europe. The high geopotential centre located over the northern sector of continental Europe favoured this large-scale flow. In contrast, the geopotential gradient was much weaker to the south, covering part of Morocco, Algeria and the western Mediterranean.

In direct connection with the genesis of stormy weather over the Balearic Islands, a cold cut-off low of small dimensions (diameter of about 600 km) was present at the same mid-tropospheric level over the Iberian Peninsula and its Mediterranean coast. This disturbance is well marked in the synoptic map and implies a southerly flow over the western Mediterranean, especially along its eastern flank. The depression was associated with a positive vorticity anomaly to the south-southwest that was advected by the mid-level winds towards the position of the Balearics and the northeastern lands of the Iberian Peninsula.

This classical synoptic pattern, when combined with a low-level moisture feeding mechanism and convective or latent instability in the atmospheric column, is known to be conducive to heavy precipitation in Mediterranean Spain (Doswell et al., 1998; Romero et al., 1999).

Surface isobars (white contours in Fig. 2a) reveal, in addition to the low-pressure centres of the North Atlantic, a powerful anticyclone over Eurasia that covered most of the Mediterranean and determined a general flow from the southeast in the western Mediterranean region. This maritime flow was most pronounced towards the Balearic Islands and the Spanish Mediterranean coast, owing to the presence of a shallow and weak depression extending from the southern half of the Iberian Peninsula towards the Atlantic coast of Africa. The synoptic situation at 850 hPa (not shown) was very similar to the surface circulation, displaying a marked warm air advection from the southeast towards the Balearic Islands. This thermal advection is confirmed by the presence of veering winds between low tropospheric levels and 500 hPa. The humidity records taken at the main meteorological stations of the western Mediterranean (not shown) reveal that the air advected towards the Balearic Islands also had a high moisture content, thus helping to develop latent instability conditions over the western Mediterranean. In addition, the persistence of this warm and moist flow during October 9 was most likely instrumental in sustaining the convective systems once initiated.

Figure 2b shows the IR satellite image at 1700 UTC (1900 h Local Time; hereafter LT), that is, at the time the torrential rainfall was occurring over the study area (see Fig. 3a and 3d). This image clearly shows the cloud structure associated with the upper-level cold low, a plume extending from North Africa along the western Mediterranean with embedded intense convective nuclei. Several convective cores stand out with very cold tops to the south and above the Balearic Islands, illustrating the powerful character and high depth of the convective cells. During previous hours (images not shown), several convective clusters could already be identified to the south of the Balearic archipelago. These systems then moved northwards, affecting north of Mallorca and west of Menorca during the afternoon and evening hours. Figure 3d shows how the precipitation evolved



in response over the affected area. These extreme accumulations from a sequence of mature storms repeatedly affected the northeast of Mallorca.

130 The fact that the convective systems formed east of the small cut-off low identified at 500 hPa (see Fig. 2a and 2b) is consistent with the dynamical influence attributed to these isolated cold disturbances: the eastern flank is the zone with the most favoured upward motion across a deep column and, therefore, the preferential area for an organized and intense release of convective instability. Since these convective nuclei developed over the sea, the trigger mechanisms most likely consisted of some sort of low-level convergence line defined by mesoscale factors ahead of the above-mentioned southeasterly current.

### 2.3 Atmospheric modelling and convective precipitation predictability

135 An initial numerical exploratory study was performed after it was ascertained that no operational system forecasted precipitation rates over eastern Mallorca anywhere near the recorded rainfall rates (Figs. 2c and 2d) in their operational cycles. A mesoscale (900 m) and a microscale (100 m) domain were defined, centred over the Balearic Islands and the Sant Llorenç basin respectively, with attention paid to the possible hydrological and hydraulic modelling, and so accounting for coupling requirements. Atmospheric numerical simulations for this event are produced with the Weather Research and Forecasting (WRF) Model, version 3.9, and are initialized with different ECMWF operational products. The WRF configuration is a standard suite of parameterizations used by Amengual et al. (2017) and also described at <https://meteo.uib.es/wrf>.

140 A first set of experiments consisted of nesting the WRF domains in the deterministic high resolution (~9 km horizontal) ECMWF atmospheric model using the 00 and 12 UTC 8 Oct (0200 and 1400 h LT), and 00 UTC 9 Oct operational cycles. Although all three simulations show precipitation accumulations exceeding 100 mm somewhere in the region, none of them produced rainfall above 50 mm for the afternoon and evening of October 9. This reveals the presence of forecast errors from sources other than the resolution limit.

145 To account for uncertainties in initial conditions of the simulations, and to examine the potential guidance that dynamical downscaling of the 50 members of the ECMWF EPS could provide for this case, the WRF runs were nested in the 00 UTC October 9 operational cycle. The 12h-accumulated precipitation valid at 00 UTC 10 Oct for all members showed a high diversity of possible scenarios but none of them showed enough ability to have triggered dependable warnings over the affected area. Indeed, the field of probability of 12 h-accumulated precipitation above 100 mm focused attention over the western side of the domain, with only marginal probabilities over the eastern sector of Mallorca and negligible odds at the Sant Llorenç catchment (Fig. 2c). Likewise, when model errors are also considered by activating stochastic perturbed parameters in the boundary layer and land surface parameterizations in WRF (Jankov et al., 2017), location and intensity of predicted torrential rain cells are not significantly improved (not shown). However, regarding precipitation amounts and the usable limits of these 12 to 24 h forecasts for early warnings and civil protection awareness, these exploratory ensemble prediction systems show the possibility of maximum 12 h accumulations exceeding 250 mm at distances below 30 km from the St. Llorenç catchment for this particular event. Given the above-mentioned characteristics of the catchment and the fairly typical location errors of

determinant convective cells obtained for this case, these state-of-the-art sub-kilometric ensemble predictions may well illustrate a serious predictability limit of precipitation structures usable in hydrological forecast systems over 12 to 24 h lead times.

### 3. Methods

#### 3.1 Precipitation analysis

The Doppler C-band weather radar located at Palma airport (50 km away from Sant Llorenç) performs volume scans with spatial and temporal resolutions of 1 km and 10 minutes, respectively. Quantitative rainfall estimations were derived from the radar volumetric reflectivity scans on October 9, 2018. Partial beam blocking was corrected using the procedure developed by Pellarin et al. (2002). Next, the WSR-88D convective relationship was used to convert the 10 minutes radar reflectivity to precipitation estimates (Hunter, 1996). Finally, the radar-based hourly rainfall accumulations were compared against observations from the automatic weather stations of the Spanish Meteorological Agency (AEMET). Errors in hourly radar estimates were corrected by applying a dynamical adjustment (Cole and Moore, 2008).

Once inaccuracies in the hourly radar-derived rainfall estimates were amended, the 24 h cumulative amounts were verified against the daily precipitation accumulations recorded at all pluviometric stations. The scatterplot of total rainfall amounts observed by both measurement networks shows an excellent agreement (Fig. 3b). Squared correlation coefficient is slightly above 0.98 and radar-derived precipitation features a small positive bias of 2.5 mm when averaged over the 21 rain gauges. The spatial signature of the moving train of convective cells precipitating over the same region is clearly visible from the distribution of accumulated radar-derived precipitation (Fig. 2c and 3a). The train of convective cells followed a south-to-north direction, affecting Sant Llorenç basin from 13 h to 20 h UTC (15 h to 22 h LT) on October 9, 2018. Maximum rainfall intensities lasted from 14 h to 18 h UTC (16 h to 20 h LT) over this catchment.

A comparison of the areas over which a given amount of accumulated precipitation was exceeded, according to the rain gauges and radar, reveals that the sampling characteristics of the former network were not small enough for a correct delineation of the heavy rainfall areas (Fig. 3c). The highly local spatial scale at which heavy rainfall developed prevented its suitable observation by the relatively dense but irregularly distributed pluviometric network (Marchi et al., 2010).

Exceedance areas were computed over the land mass of the radar spatial domain considered in Figure 3a. This inland region has a whole extension of 618.0 km<sup>2</sup> and a pluviometric density of 29.4 km<sup>2</sup>. The spatial distribution of the cumulative precipitation observed by the rain gauge network was obtained after applying kriging with a linear model for a semivariogram fit. While the weather radar delineated heavy rainfall areas close to 10 km<sup>2</sup>, the pluviometric network captured regions one



order of magnitude larger (~100 km<sup>2</sup>). Therefore, the actual rain gauge network observed exceedance areas impacted by heavy  
190 precipitation up to 200 mm, while radar estimates rendered amounts up to 350 mm for the October 9, 2018 episode (Fig. 3c).

### 3.3 Hydrological modelling

The Flood Event–Based Spatially Distributed Rainfall–Runoff Transformation–Water Balance (FEST-WB) model was  
implemented to assess the hydrological response of Sant Llorenç catchment to the torrential precipitation. FEST-WB is fully  
distributed and physically based, accounting for evapotranspiration, infiltration, surface runoff, subsurface flow and flow  
195 routing (Rabuffetti et al., 2008). The hydrological model computes soil moisture fluxes by solving the water balance equation  
at each grid point. The evolution of soil moisture ( $\theta_{ij}$ ) for the grid point at (i, j) is given by:

$$\frac{\partial \theta_{ij}}{\partial t} = \frac{1}{Z_{ij}} (P_{ij} - R_{ij} - D_{ij} - ET_{ij}) \quad (1)$$

200

where P is precipitation rate, R and D are runoff and drainage fluxes, ET is evapotranspiration rate, and Z is soil depth. Runoff  
is calculated according to a modified Soil Conservation Service–Curve Number (SCS-CN; USDA, 1986) method extended for  
continuous simulation (Ravazzani et al., 2016). That is, the maximum potential retention S is updated at the beginning of a  
205 storm as a linear function of the degree of saturation ( $\varepsilon$ ):

$$S = S_1(1 - \varepsilon) + S_3\varepsilon \quad (2)$$

210

where  $S_1$  and  $S_3$  are the values of S when soil is dry and wet (i.e., antecedent moisture conditions I and III, respectively). The  
actual evapotranspiration is calculated as a fraction of the potential rate tuned by the beta function that, in turn, depends on  
soil moisture content (Montaldo et al., 2003). Potential evapotranspiration is computed according to a modified version of the  
Hargreaves–Samani equation (Ravazzani et al., 2012). The surface and subsurface flow routing is based on the Muskingum-  
215 Cunge method (Chow et al., 1988).

To better cope with the strong nonlinearities of the rainfall-runoff transformation, model calibration focussed on calibrating  
infiltration storativity ( $S_0$ ) and the initial abstraction ratio ( $\lambda$ ). Calibration of  $S_0$  permits proper reproduction of the observed  
flood water balance when using CN spatial distribution, while calibration of  $\lambda$  copes with the specific lithological features of  
the examined watershed (Borga et al., 2007).



- 220 Parameter adjustment relied on post-event surveys of peak discharge and flow velocity. Heterogeneities in the hydraulics of the Sant Llorenç catchment response to the October 9, 2018 flash flood were also taken into account. These heterogeneities emerged as result of the gradual decrease of catchment response to increased rainfall amounts. The main factors regulating these heterogeneities are the expansion of the stream network to not previously channelled topographic elements and the increase of flow velocity with discharge (Borga et al., 2007).
- 225 FEST-WB was forced by using hourly rainfall and daily temperature data from August 1, 2018 00 UTC to October 9, 2018 00 UTC. This warm-up period allows a reliable initialization of the soil moisture content for Sant Llorenç catchment. Next, the hydrological model was driven by the 10-min radar precipitation fields from 9 to 10 October 2018 00 UTC. A multisite calibration was performed to account for the acute nonlinearities in the rainfall-runoff conversion (Amengual et al., 2017). Heterogeneities in the hydraulics were calibrated through basin canalization and hillslope (vhs) and channel (vc) flow velocities
- 230 through the Strickler coefficients (Table 1).

### 3.4 Hydraulic modelling

The U.S. Army Corps of Engineers' River Analysis System (HEC-RAS) was used for hydraulic modelling and flood mapping, a software that allows 1-D steady and unsteady flow hydraulics calculations (US Army Corps of Engineers, 2016). In this study, HEC-RAS unsteady flow analysis was implemented to obtain flooding water extent and timing, water maximum depth

235 and water maximum velocity during the event. 1-D hydraulic models replicate water movement by solving equations formulated by applying laws of physics. More specifically, HEC-RAS solves equations derived by ensuring mass conservation (Equation 3) and momentum conservation (Equation 4) between two cross-sections  $\Delta x$  apart, which yields the one-dimensional Saint-Venant equations:

240 
$$\frac{\partial Q}{\partial x} + \frac{\partial A}{\partial t} = 0 \quad (3)$$

$$\frac{1}{A} \frac{\partial Q}{\partial x} + \frac{1}{A} \frac{\partial (\frac{Q^2}{A})}{\partial x} + g \frac{\partial h}{\partial x} - g(S_0 - S_f) = 0 \quad (4)$$

where  $Q$  is flow discharge ( $Q = uA$ , where  $u$  is cross-sectional average velocity and  $A$  is flow cross-section area),  $t$  represents

245 time,  $h$  is water depth,  $g$  is gravitational acceleration,  $S_f$  is frictional slope, and  $S_0$  is channel bed slope (US Army Corps of Engineers, 2016). Although equations (3) and (4) have no analytical solution, they can be solved using numerical techniques, allowing the estimation of  $Q$  and  $h$  for every cross-section at each time step (Teng et al., 2017).

The HEC-RAS model was chosen because, in terms of predictive analysis, it performs better than more sophisticated models (e.g. TELEMAC, LISFLOOD-FP) and has fewer data requirements (Horritt and Bates, 2002; Teng et al., 2017). HEC-RAS



250 can also be adequately calibrated on hydrometric data and has proved to accurately predict flood extent when water surfaces are superimposed onto accurate high-resolution digital elevation models (DEM). For these reasons, HEC-RAS has been applied worldwide for flood simulation purposes, especially in locations highly prone to suffer flash floods, including Vietnam (Nguyen et al., 2015), Malaysia (Alaghmand et al., 2012), Pakistan (Khattak et al., 2016), Turkey (Curebal et al., 2016), Greece (Papaioannou et al., 2016), Spain (Ruiz-Villanueva et al., 2013) and Texas (Knebl et al., 2005).

255 In order to provide HEC-RAS with reliable topographical information to accurately delineate the cross-sections needed to set up the hydraulic model, a LIDAR (Laser Imaging Detection and Ranging) derived Triangular Irregular Network (TIN) was generated to extract detailed floodplain topography. To do so, eight 2x2 km sheets of LIDAR point clouds from the Spanish National Geographic Institute ([http://centrodedescargas.cnig.es/CentroDescargas/locale?request\\_locale=en](http://centrodedescargas.cnig.es/CentroDescargas/locale?request_locale=en)) were obtained, covering Sant Llorenç town and its surroundings upstream, with an average point spacing of 0.82 m. A 1 m resolution DEM  
260 based on the returns of the laser beams generated by bare ground, buildings and roads was then created. However, due to the noise contained in some LIDAR point clouds, cross-sections and river bed elevations, based on LIDAR-derived DEMs, artefacts which may cause underperformance of the hydraulic model could be introduced. To avoid this, a TIN using detailed contours (delineated at intervals of 1 m) of the LIDAR-derived DEM was generated, which serves to better define floodplain topography for flood simulation purposes, since TIN-derived cross-sections present smoother curves (Costabile and  
265 Macchione, 2015). The HEC-RAS model was set up using 40 cross-sections distributed along the 4303 m of reach length, to provide the model with information on channel width and bed elevation (examples of these sections and bed elevation profiles are shown in Fig. 6). The number of cross-sections was limited by the meandering shape of the Ses Planes river at Sant Llorenç and the extraordinary extent of flooding in the city centre (cross-sections wider than 300 m were required to cover the affected areas at some points), since cross-sections could not intersect each other. For bridge modelling, two additional cross-sections  
270 were defined, located immediately upstream and downstream of each of the seven bridges crossing Ses Planes stream channel in Sant Llorenç town.

Upstream boundary conditions for the simulation were imposed by the modelled discharge hydrograph at the first cross-section, and downstream boundary conditions were imposed by the frictional slope calculated empirically from TIN-derived river bed slope between cross-sections. Manning's  $n$  roughness coefficient values (Table 2) were based on CORINE land cover  
275 data from 2018 and adapted following Papaioannou et al. (2018). Detailed topographic information on floodplain was set up for the analysis using HEC-GeoRAS extension for ArcGIS®, and we depurated the topographic and geometric information using HEC-RAS software in an iterative fashion. This process included the depuration of topological errors in river banks and hydraulic incongruities at bridges, and the filtering of cross-section delineating points.

For dynamic reconstruction of the flash flood (i.e., its timing and the spatial extent of flood-affected areas), HEC-RAS unsteady  
280 flow analysis was applied. The plan established for this flash flood simulation started at 1700 h and ended at 2400 h (LT) on October 9, ensuring that the entire event, as modelled by the discharge hydrograph shown in Fig. 4, was encompassed within the analysis. The computation time step was set up at 10 minutes (same temporal resolution as the discharge hydrograph) and the output time interval was set at 1 minute, although only flooding maps every 10 minutes are shown (Fig. 4). Validation of



the results was made by comparing the simulated flooded area with the observed event by Copernicus Emergency Management  
285 System (Sentinel-1 imagery), and the modelled water depth was compared with flooding marks measured in-situ a few days  
after the event.

### 3.5 Evaluation of flash flood magnitude and geomorphological impacts

In order to contextualize the exceptionality of this flash flood and for comparison purposes, a power metric that summarizes  
the magnitude of the event was used. One option for quantifying the power of moving water that drives sediment transport and  
290 geomorphic change is the unit stream power ( $Wm^{-2}$ ). It is computed as

$$\omega = \frac{\gamma QS}{w} \quad (5)$$

where  $\gamma$  is specific weight of water ( $Nm^{-3}$ ),  $Q$  discharge ( $m^3s^{-1}$ ),  $S$  is friction slope ( $m/m$ , here equal to the channel slope).  
295 These three components are the total stream power ( $\Omega$ ) that is normalised by peak flow width ( $w$ ; Bagnold, 1966).

For assessment of the geomorphological effects of the event, several remote sensing techniques were used. First, two false  
infrared RGB (red, green and blue) composites (Fig. 7a and 7b) of Planet® high resolution (3 m pixel size) spectral imagery  
were visually compared, acquired hours before and the day after the event. In these image composites, the band corresponding  
to short wave infrared (SWIR) is set to the red channel. Thus, the increasing signal of the red channel (pink) in the image after  
300 the flash flood denotes a rise in the responsive signal of pixels corresponding to bare soil, rocks and sediment (Lillesand et al.,  
2015), suggesting the occurrence of strong runoff processes with associated mudflow and sediment erosion and transport.  
Consequently, a huge amount of debris was deposited in several new gravel and coarse sediment bars along the Ses Planes  
torrent floodplain. An estimation of the sediment deposited was made using a very high resolution DEM (6 cm pixel size) and  
orthophotograph (3 cm pixel size) calculated using Structure from Motion (SfM) techniques (Schumann et al., 2019). Both  
305 corresponded to an external Unmanned Aerial Vehicle (UAV) photogrammetric flight (Garau Ingenieros®) from November  
2018.

For quantification of sediment extent, a two-step approach was used, based on this very high resolution imagery and elevation  
data. First, image spectral analysis was used to differentiate among different cover types, and an interactive supervised  
classification was performed, manually defining the training samples on the RGB bands of the orthophotograph (Camenen et  
310 al., 2013). Spectral-based classification performed well when classifying vegetation types and water cover, although sediment  
spectral responses in the RGB bands were not distinguishable enough to correctly discriminate between sediment types (not  
shown). To overcome this, the procedure described in Carbonneau et al. (2005) was followed, using texture as an indicator of  
sediment type and its spatial patterns. Orthophotograph pixels were evaluated in a Grey Level Co-occurrence Matrix (GLCM),  
used to quantify how many pixels of similar grey levels are neighbours. This windowing (kernel) approach generates a textural  
315 image which retains local image texture properties using contrast calculation and allows classification of pixels into different



types (land covers) based on very high resolution (3 cm in this case) image. This textural image was used to accurately classify land cover into six categories (trees, shrubs, herbaceous vegetation, water, fine sediment and coarse sediment) by means of an interactive supervised classification (manually defining the training samples on the textural image). More details about GLCM calculation can be found in Carbonneau et al. (2005).

320 Once the extent of the sediment deposited during the event was obtained, the height of the event-created gravel bars and deposits were estimated by subtracting the height of each pixel in the LIDAR-derived DEM (data acquired before the event) from those in the SfM-derived DEM (data acquired less than one month after the event; Fig. 7c and 8). For volume calculation, the base area (each 6 cm<sup>2</sup> pixel) was multiplied by the height of each sediment bar pixel calculated before. In this way, each (2-D) pixel has an associated (3-D) volume which corresponds to the column above it and is defined by pixel bar height (a  
325 rectangular prism in which the base is the square pixel and the side is the height value). To compute an estimation of bar sediment weight, the volume raster layer per rock density (2700 kg/m<sup>3</sup> for limestone) and porosity of the deposit (15%) were multiplied.

## 4. Results

### 4.1 Precipitation estimates

330 Figure 3a shows the modelled accumulated precipitation during the day of the flood event in northeast Mallorca, where the affected catchment is located. Radar-based estimates of precipitation were compared to rain gauge observations, showing great agreement ( $R^2 = 0.98$ , Fig. 3b). It can be concluded that an area larger than 100 km<sup>2</sup> (Fig. 3c) was affected by an intense rain of 200 mm, with increasing values towards the centre of such area, reaching peaks of 350-400 mm in the upper parts of the San Llorenç catchment, which features fan-shaped topography (Fig. 3a). This part of the catchment lies within the isohyetal  
335 line of 300 mm and, with an extension about 10 km<sup>2</sup> functioned as a funnel, gathering the precipitation and generating intense runoff processes that rapidly accumulated flow into the well-developed hydrological network. The precipitation event lasted six hours (from 1400 h to 2000 h LT approx.), which gives an average intensity of around 60 mm per hour. However, peak rainfall exceeded 100 mm/hour in the moments previous to the flood event, with 140 mm falling between 1840 h and 1940 h (LT) that added up to the 130 mm fallen in the previous hours (Fig. 3d). The aforementioned synoptic conditions that generated  
340 a succession of convective nuclei over the area were responsible for this precipitation event. The question that remains is why such amounts of precipitation fell over that catchment and not on nearby areas. Two hypotheses may explain this phenomenon: the existence of a stationary convergence line that favoured convection on that particular south-north fringe; the anchoring effect of orography, slowing down the movement of the convective cell train. The mountains of the catchment are, however, not high enough to produce such an anchoring effect, so perhaps the role of orography was limited to just enhancing the  
345 convection uplift as the convective cells moved northwards.



## 4.2 Coupling hydrological and hydraulic modelling of the event

After calibration with *in-situ* measurements, FEST-WB simulated peak discharge of  $306.88 \text{ m}^3\text{s}^{-1}$  at the entrance of Sant Llorenç town, which is close to the expected discharge for a 500-year return period ( $347.9 \text{ m}^3\text{s}^{-1}$ ) and depicts a specific peak discharge of  $13.11 \text{ m}^3\text{s}^{-1}\text{km}^{-2}$  (Fig. 4). The extremely sharp rising limbs denote a very fast peak (50 minutes), which may be explained by several factors: sparse and low density vegetation, very steep slopes, thin soils, watershed topography with a bottleneck in its medium reaches, etc (Fig. 1). Such characteristics, together with the overwhelming rainfall intensity resulted in fast Hortonian flows, and favoured the rapid generation of streamflow with very short runoff concentration and lag times, increasing the hazardous component of the forthcoming flood. According to the hydrological simulation, peak occurred at 1920 h (LT) in the reach 2 km upstream of Sant Llorenç and at 1930 h (LT) at the entrance of town. Because extensive overflowing was observed at the river entrance to Sant Llorenç town, the simulated runoff hydrograph at this point has been used to force the hydraulic model. Therefore, direct comparison of simulated against estimated water levels at different locations in the town, surveyed during the post-flood field campaign, were used as a verification check of the estimated discharges.

Almost 400 mm of rainfall accumulated in barely six hours in the fan-shaped headwaters of the watershed. In spite of water loss via infiltration, a significant amount of overland flow was rapidly routed into the river network and streamflow, which was inconsequential minutes before, rapidly increased. Hydrological modelling depicts a peak flow close to  $307 \text{ m}^3\text{s}^{-1}$  at 1930 h (LT) at the entrance of Sant Llorenç town just 20 minutes after the start of the episode, with no initial baseflow (Fig. 4). The hydraulic simulation (Fig. 4) shows how water starts flowing through Sant Llorenç town at 1900 h (LT) and, in barely 10-20 minutes, it starts overflowing the artificial channel at several points within the sector between bridge #2 and bridge #3, reaching depth values of about 3 m. The football field locate in the meander between bridge # 2 and bridge # 3 was completely flooded in less than half an hour. It only takes between 10 and 20 minutes for the peak flow modelled at the entrance of the town to reach the maximum extent of flooded area in the city centre: water covers the entire longitudinal path of the channel through town, with the most affected areas in the vicinities of bridges and river corners. The major peak wave entered the northern sector of the town centre around 1940 h (LT), completely overflowing bridge #2 and adjacent areas and began to flood the Town Hall square (the very town centre) with around 0.50 m of water. As the peak flow wave moved southwards, the southern sector of the town centre between bridge #3 and bridge #4 was severely affected. Water depth reached almost 1.5 m in the Town Hall square and the surrounding blocks, which are located 150-200 metres away from the main river channel. After 2000 h (LT) the floodwaters receded from most of the town, except for an area located between bridge #2 and bridge #3, which remained flooded until 2030 h (LT) due to the backwater effect of bridge clogging and the wide open topography of the surrounding non-built area.



### 4.3 Flood simulation and flood area mapping

Simulated water depths from modelled discharge and detailed flood extent are depicted in Figure 5. For comparison purposes, included is the observed flooded area by Copernicus Emergency Management System (via Sentinel 1 radar imagery) and compared simulated water depths with observed flooding marks from on-site field measurements (Fig. 5d). These show a high correlation coefficient ( $R^2 = 0.91$ ), indicating good performance and reliability of the hydrological and hydraulic simulations.

380 Figure 5a shows how the simulated flooded area mostly corresponds to that estimated via satellite, except for one section located about 800 m upstream of the town entrance. This is explained by the flood breaking down a stone wall and inundating the lands beyond, and this was not accurately reproduced by the hydraulic simulation. Figure 5a also shows the area corresponding to theoretical floods with return periods of 10, 100 and 500 years, given by the Spanish Ministry of Agriculture, Food and Environment for this particular area (MAPAMA, 2010). The estimated flooded area by both our hydraulic modelling and the observed event by Copernicus Agency goes far beyond the floodplain with a 500-yr return period, indicating the exceptional nature of this event. The detailed maps (Fig. 5b and 5c) show that the inundated areas near the channel, which included residential buildings, reached water depths close to 2 m (this was corroborated with in-situ measurements inside the houses of various residents). The most affected areas were those located between bridges and channel corners, due to the clogging effect they exert on water flow. Of note is the great extension of the flooded area inside the town (up to 100 m from side to side in some areas), compared to that which occurred upstream in agricultural lands (around 60 m width), as section plots in Figure 6 depict. This can be explained by several factors: the aforementioned effect of bridges and channel corners which blocked the water and the transported sediment and debris; the topography, as the town is located in the flattest (therefore susceptible to be flooded) area; and finally, the effect of concrete and pavement, which prevents infiltration and increases the kinematic energy of the water body and therefore the destructive power of the flood. This is very well observed in Figure 6, where water velocity from the simulation is depicted. The water flows down the natural riverbed up to where bridge #2 is located, and where the concrete artificial channel starts (note that the artificial channel capacity is  $161.5 \text{ m}^3\text{s}^{-1}$ , whereas a flood peak discharge of  $307 \text{ m}^3\text{s}^{-1}$  was estimated). That location also coincides with a  $105^\circ$  turn in the riverbed as it is canalised; therefore, the water is forced to turn and pass through a narrower section, where the roughness of the riverbed greatly decreases.

395 The consequence of this is a vast increase in velocity from roughly  $2 \text{ m s}^{-1}$  before the corner to  $7 \text{ m s}^{-1}$  after the corner. From there, the topography opens up to a plain zone where water floods and velocity decreases. The other major increase in velocity occurs right after the second corner upstream of bridge #3. The bridge (pictured in Figure 6), which occupies more than half the flooded section, blocks the water and increases its velocity upstream due to flux accumulation and generation of intense backwater effects caused by bridge clogging. The same happens upstream of the other bridges (minor orange-red spots in Fig. 6) but of a smaller magnitude.

400  
405



#### 4.4 Flash flood magnitude and geomorphological impacts

The estimated peak discharge, close to  $307 \text{ m}^3\text{s}^{-1}$  for a  $23.4 \text{ km}^2$  catchment, has a corresponding unit peak discharge of  $13.11 \text{ m}^3\text{s}^{-1}\text{km}^{-2}$ , and a lag time of 30 minutes, which fits well with the relationship between lag time and catchment area proposed by Marchi et al. (2010) for areas  $< 350 \text{ km}^2$ :

$$T_L = 0.08A^{0.55} \quad (6)$$

with a result of 0.45 hours (27 minutes). Note that lag time has been computed as the time difference between the net rainfall and runoff centroids. The unit stream power obtained for the natural flooded section was  $1110 \text{ Wm}^{-2}$ . The value can be considered in the upper range for this type of small catchment with medium-high slopes. The magnitude of the flash flood impacted the channel, changing its morphology. The geomorphological effects are shown in Figure 7. High resolution satellite images before and after the event show the impact over a 4.4 km channel upstream of the village. A volume of  $14000 \text{ m}^3$  of sediment (5671 metric tonnes) was deposited as new bars, especially on the meanders. The sediment was composed of gravel and fine material, with sporadic blocks on top of some deposits. There are areas with a maximum sediment depth of 1 m. The flash flood eroded sediment from agricultural fields on the headwaters, especially on those located over softer lithology (Cretaceous marls and limestones) in the western area. The flood also eroded shrubs and numerous trees along the channel. Fig. 8 shows what occurred in the largest meander on the studied reach. The concave area of the meander facilitated deposition of a large amount of transported sediment, although woody debris enhanced the aggradational process. The original main channel moved 30 m northwards after the flash flood, with a deposition of more than 1000 tonnes of sediment in a new fluvial stream bar (Fig. 8c). Comparing Figures 8a and 8b, it is possible to identify how several trees disappeared after the flood. The new bar created by the flash flood is up to 200 m length and around 65 m width, reaching 1 m depth at some points. This new channel created after the flash flood is a clear example of the geomorphological effects of this large magnitude event.

## 5. Discussion

### 5.1 Predictability and hydro-meteorological modelling issues

This singular case exemplifies the complex challenges faced by scientists, hydro-meteorological forecasters, civil protection managers and policy makers in predicting Mediterranean flash floods. Without a doubt, the main challenges of prediction in this instance were the small spatial and temporal scales of multiple elements, which contributed specifically to the tragic urban flood of October 9, 2018 at Sant Llorenç. Determinant precipitation structures at the sub-kilometric scales in the convective systems affecting the eastern Balearic Islands were identified in previous sections, impacting the hydrological catchment. Indeed, observed precipitation rates in this case are high but not extreme and even fairly common in the area. This fact



dismisses most climatology-based prediction methods for this case. Statistical methods to forecast precipitation fields from historical records, such as analogs (Hamill et al., 2006), pattern-based (Nuissier et al., 2011) or statistical downscaling of large scale forecasts (Wilks, 2010) are worthless for the warning protocols over useful forecast ranges. The inability of the first preliminary numerical tests to sufficiently indicate the location, intensity and timing of the precipitating systems responsible  
440 for the tragic floods on October 9, 2018 in the village of Sant Llorenç, outlines important challenges and research questions for the hydro-meteorological communities. The development of a successful flash flood warning system for the region will take many years and will face fundamental predictability topics and require the collaborative efforts of researchers across fields to succeed. Any dependable hydro-meteorological forecasting system candidate for this event must combine sub-kilometric precision in the precipitating systems, decametric precision in the hydrological modelling and metre or sub-metre precision in  
445 the hydraulic component of the forecasting chain. These ambitious spatial requirements are linked to, and thus also determine, the temporal scales accounted for in each modelling phase.

## 5.2 Radar-derived rainfall estimates and modelled hydrograph

Despite predictive models failing to foresee and reproduce the huge amount of precipitation recorded in the north-eastern part of Mallorca during October 9, 2018, we were able to accurately estimate it using radar information. However, the high spatial  
450 variability and uncertainty associated with convective storms introduces limitations when deriving precipitation estimates with radar at long distances (Burcea et al., 2018). Fortunately, in this study, the Doppler weather radar was 50 km from the catchment, allowing us to obtain very accurate precipitation estimates ( $R^2 = 0.98$  between radar-derived and observed precipitation). This is important, since the region features an unevenly distributed meteorological network and, more specifically, for the studied catchment which, despite several flash floods over the last decades, still lacks weather and gauging  
455 stations for rainfall and streamflow data recording. Accurate reproducibility of precipitation amounts generated by intense convective rainfall episodes in ungauged catchments, using radar data, as presented here, represents a significant contribution for regions with sparse or uneven distribution of meteorological stations. Nevertheless, for meeting early warning purposes, it is necessary to reduce processing time and facilitate access to near real-time information broadcasting. This is operatively complex and implies investment, in both working force and in funding.

460 The total precipitation volume during the event, with an areal-basin average close to 317 mm, was three times larger than the monthly climatological precipitation (climatic average 1974-2014) for October, recorded in the nearby town of Artà (100 mm  $\text{yr}^{-1}$ ), and just half of the annual climatological precipitation (696 mm  $\text{yr}^{-1}$ ). Furthermore, it clearly surpasses the daily precipitation value with a return period of 500 years, estimated by the local government of Mallorca island (DGRRHH, 2001), of 210 mm  $\text{day}^{-1}$  for that particular area, indicating the exceptional nature of the event. These very accurate radar-derived  
465 precipitation estimates were the main input of the FEST-WB model, and this is a vital step in the reconstruction of the event. The robustness of the method used and the accuracy of the estimations increased the reliability of the hydrological modelling and the hydraulic simulation.



The modelled hydrograph depicted a peak flow of  $307 \text{ m}^3\text{s}^{-1}$ , which corresponds to a peak specific discharge of  $13.11 \text{ m}^3\text{s}^{-1}\text{km}^{-2}$ . These figures are similar to those recorded in other catastrophic flash floods that have occurred in the Mediterranean basin. 470 Delrieu et al. (2005) highlighted peak specific discharges between  $10$  and  $30 \text{ m}^3\text{s}^{-1}\text{km}^{-2}$  in several watersheds of the Mediterranean Gard region in France (the so-called *Gard event*) during a catastrophic flash flood event that occurred on September 8 and 9, 2002. This flood was at a larger scale (in terms of rainfall amount and the extent of the affected areas) than the flood in Sant Llorenç. Furthermore, the peak specific discharge of  $13.11 \text{ m}^3\text{s}^{-1}\text{km}^{-2}$  registered at Sant Llorenç is one order of magnitude bigger than that recorded by Tarolli et al. (2012) in selected Mediterranean small- and medium-sized basins of 475 Italy, France and Spain.

The hydrograph modelled in this study, with a very steep rising limb and fall in less than two hours, is similar to hydrographs of significant flash floods near Mallorca, such as the region of Valencia (Camarasa-Belmonte and Segura-Beltrán, 2001), the Gredos Range in central Spain (Ruiz Villanueva et al., 2014), or the lower reaches of the Guadiana basin (Ortega and Garzón-Heydt, 2009); however, in most cases, both absolute and specific discharge were much lower than in the event registered at 480 Sant Llorenç.

### 5.3 Hydraulic simulation performance

The hydraulic simulation performed with HEC-RAS was evaluated in two ways: first, it was confirmed that the simulated extent of the flood was very similar to the extent delineated by Copernicus Emergency Management System, based on Sentinel-1 radar imagery. The main differences were underestimation of modelled flood extent in the reach immediately before the entrance of Sant 485 Llorenç, due to a break in a wall, and the greater extent of the modelled flood in the northeastern quadrant of the town centre compared to the observed event by Copernicus. The latter may not be an overestimation of the simulation, since several Sant Llorenç locals confirmed that those areas were flooded during the event. Second, 32 in-situ after-event measurements (flooding marks) were compared with modelled depths, obtaining good agreement ( $R^2 = 0.91$ ), so it can be concluded that hydraulic simulation forced with the modelled discharge hydrograph was very accurate in terms of flood spatial extent delimitation (Papaioannou et al., 2016). 490 Flow velocity simulations introduce more uncertainties since we cannot verify the results by comparison with direct measurements. However, the figures obtained (maximum flow velocity at bridge surroundings of  $7 \text{ m s}^{-1}$ ) are consistent with Ruiz Villanueva et al. (2014), who obtained flow velocities above  $3 \text{ m s}^{-1}$  with a peak flow discharge of  $120 \text{ m}^3\text{s}^{-1}$  (less than half of the estimated peak discharge) in a catchment of  $15.5 \text{ km}^2$  in central Spain. They also observed how velocity highly increased at bridge locations and generated intense backwater processes. Additionally, Yalcin (2018) simulated maximum velocities around  $4 \text{ m s}^{-1}$  for an expected 495 peak flow of  $25 \text{ m}^3\text{s}^{-1}$  in a  $11 \text{ km}^2$  catchment in central Turkey. In this context, the use of the 1-D approach for analysis of bridge effects may not properly simulate the interactions between bridge and flow, and backwater effects may be underestimated or neglected (Costabile and Macchione, 2015). This seems to not be the case for Sant Llorenç since water velocity greatly increased at bridges, and sections between bridges #2 and #3 were flooded for a longer time, denoting that the model registered the occurrence of intense backwater processes at these bridge locations.



#### 500 **5.4 Flash-flood magnitude and geomorphological impacts**

The peak discharge, the unit peak discharge and the lag time give an idea of the extraordinary and sudden character of the flash flood that occurred in this ephemeral stream. The unit stream power of  $1110 \text{ Wm}^{-2}$  is related to bank erosion and deposition and to the risk of substantial channel widening or major geomorphic change (Yochum et al., 2017). This value is similar to other flash flood events which caused a major geomorphic response in an alluvial channel (Marchi et al., 2016), reported for  
505 small streams in the Mediterranean climatic region. Although the studied stream features steep slopes (2.24 % average) and has an area of  $23.4 \text{ km}^2$ , others with similar areas reported one order of magnitude more on unit stream power (i.e., Baker and Costa, 1987; Batalla et al., 1999).

After the flood, a significant trend in channel widening was observed, similar to other stream floods (Righini et al., 2017), with a large accumulation of gravel and fine material in new fluvial bars. The accumulation of woody debris decreased  
510 transport capacity, and flow obstruction by vegetation created positive feedback for instream aggradation (Merritt and Wohl, 2003; Ruiz-Villanueva et al., 2013). Along the study reach, several trees were eroded, transported and deposited downstream, arriving at the first bridge at the entrance of the village, facilitating channel widening and erosion of the initial artificial channel, and also increasing the hazardousness of the flood peak wave, which featured a high destructive power (unit stream power  $> 1000 \text{ Wm}^{-2}$ ).

#### 515 **6. Conclusion and outlook**

In studying the October 9, 2018 flash flood at Sant Llorenç, it can be concluded that almost all the possible hazardous factors converged to generate this extraordinary event and its fatal consequences. Contributing factors were the inability of predictive models to foresee the convective heavy rainfall event, the synergistic effect of the storm cells' trajectory, and topography that enhanced convection in the headwaters of the catchment (insight on this matter could be provided by fine-scale numerical  
520 simulations in further research). Additional contributing factors were a very small drainage area and the short hydrological response time favoured by steep slopes, the funnel-shaped watershed, low vegetation density, and thin soils which favoured the acceleration of runoff processes. Further contributing factors were the location of the town in the floodplain of the Ses Planes torrent, artificial channelization of the stream at the entrance of the town, the presence of several bridges that acted as stoppers for flow and debris and generated intense backwater effects, a delayed red alert warning, and low awareness and  
525 conscientiousness of people (people crossed bridge#3 seconds before the water flooded the road above it; see pictures in Fig. 6). As the IPCC (2012) reported, the increase of natural risks worldwide is more related to increased vulnerability (settlements and goods located in river floodplains), socio-economic impacts (land use changes) and perception (low awareness and preparedness), rather than to increased hazardousness. This idea is corroborated with the analysis performed in this study. This extraordinary convective rainfall event ( $> 300 \text{ mm day}^{-1}$  estimated versus  $210 \text{ mm day}^{-1}$  expected for a 500-year return  
530 period), and the magnitude ( $307 \text{ m}^3\text{s}^{-1}$  modelled versus  $348 \text{ m}^3\text{s}^{-1}$  expected for a 500-year return period) and impacts of the



flood were aggravated by human-dependent factors, such as the occupation of the floodplain by dwellings and infrastructure, channelization of the stream as it crossed the town with several bridges above it, and lack of conscientiousness among population, etc. This relationship between intense rainfall events and increased hazardousness due to anthropogenic factors has become a dominant pattern in the Mediterranean region (Llasat et al., 2014) and it represents a major setback for effective  
535 flash flood predictability and warning.

A question remains with respect to both maximum lead time and precision in the characterization of the flood, linked to location, intensity and mode of the precipitating systems responsible for this tragic flood. This study, and the prediction systems considered, reveals that, for the important lead time frame of 12 to 24 h, predictability limits identified in location of threatening torrential precipitation cells point to the need for warning systems and civil protection activation protocols that can cope with  
540 forecast errors in the 30 to 50 km range. As important as it is to focus research efforts on characterizing and reducing these errors, it is also important to consider these errors in future warning frameworks to come.

*Author contributions.* CG, JLL, EMT, VH, AA, CR, and RR designed the research. AA, JLL, VH, AMF, AH, CR and RR  
545 performed the formal analysis. CG and EMT completed the field work campaign. JLL drafted the paper. JLL, AA, and AMF elaborated the figures. All authors contributed to the writing and editing of the paper.

*Competing interests.* The authors declare that they have no conflict of interest.  
550

*Acknowledgements.* This work has been sponsored by CGL2017-82868-R [Severe weather phenomena in coastal regions: Predictability challenges and climatic analysis (COASTEPS)], which is partially supported by Fondo Europeo de Desarrollo Regional (FEDER) and Secretaría de Estado de Investigación, Desarrollo e Innovación. Author A. Hermoso received funding  
555 from the Spanish Ministerio de Educación, Cultura y Deporte (FPU16/05133). The authors thankfully acknowledge the computer resources at MareNostrum 4 and the technical support provided by Barcelona Supercomputing center (RES-AECT-2018-3-0009 and RES- AECT-2019-1-0008). The authors thankfully acknowledge the spectral high resolution images ceded by Planet®. The very high resolution orthophotograph and digital elevation model were ceded by Garau Ingenieros® working in a reconstruction project promoted by Direcció General de Recursos Hídrics del Govern de les Illes Balears. The authors also  
560 want to thank the interviewed Sant Llorenç locals for their testimonies, pictures and videos taken during the event.

565



## References

- Alaghmand, S., Abustan, I., Eslamian, S. and bin Abdullah, R.: Comparison between capabilities of HEC-RAS and MIKE11 hydraulic models in river flood risk modeling (a case study of Sungai Kayu Ara River basin, Malaysia), *Artic. Int. J. Hydrol. Sci. Technol.*, 2(3), 270–291, doi:10.1504/IJHST.2012.049187, 2012.
- Amengual, A., Homar, V. and Jaume, O.: Potential of a probabilistic hydrometeorological forecasting approach for the 28 September 2012 extreme flash flood in Murcia, Spain, *Atmos. Res.*, 166, 10–23, doi:10.1016/J.ATMOSRES.2015.06.012, 2015.
- Amengual, A., Carrió, D. S., Ravazzani, G., Homar, V., Amengual, A., Carrió, D. S., Ravazzani, G. and Homar, V.: A Comparison of Ensemble Strategies for Flash Flood Forecasting: The 12 October 2007 Case Study in Valencia, Spain, *J. Hydrometeorol.*, 18(4), 1143–1166, doi:10.1175/JHM-D-16-0281.1, 2017.
- Bagnold, R. A.: An approach to the sediment transport problem from general physics, Geological Survey, Washington., 1966.
- Baker, V. and Costa, J. E.: Flood power, in *Catastrophic flooding*, edited by L. Mayer and D. Nash, pp. 1–21, Allen & Unwin; Binghamton Symposia in Geomorphology, International Series, 18., 1987.
- Batalla, R. J., De Jong, C., Ergenzinger, P. and Sala, M.: Field observations on hyperconcentrated flows in mountain torrents, *Earth Surf. Process. Landforms*, 24(3), 247–253, doi:10.1002/(SICI)1096-9837(199903)24:3<247::AID-ESP961>3.0.CO;2-1, 1999.
- Bodoque, J. M., Díez-Herrero, A., Amerigo, M., García, J. A. and Olcina, J.: Enhancing flash flood risk perception and awareness of mitigation actions through risk communication: A pre-post survey design, *J. Hydrol.*, 568, 769–779, doi:10.1016/j.jhydrol.2018.11.007, 2019.
- Borga, M., Boscolo, P., Zanon, F., Sangati, M., Borga, M., Boscolo, P., Zanon, F. and Sangati, M.: Hydrometeorological Analysis of the 29 August 2003 Flash Flood in the Eastern Italian Alps, *J. Hydrometeorol.*, 8(5), 1049–1067, doi:10.1175/JHM593.1, 2007.
- Borga, M., Stoffel, M., Marchi, L., Marra, F. and Jakob, M.: Hydrogeomorphic response to extreme rainfall in headwater systems: Flash floods and debris flows, *J. Hydrol.*, 518, 194–205, doi:10.1016/j.jhydrol.2014.05.022, 2014.
- Burcea, S., Cică, R. and Bojariu, R.: Radar-derived convective storms climatology for Prut River Basin: 2003–2017, *Nat. Hazards Earth Syst. Sci. Discuss.*, 1–30, doi:10.5194/nhess-2018-354, 2018.
- Camarasa-Belmonte, A. M. and Segura-Beltrán, F.: Flood events in Mediterranean ephemeral streams (ramblas) in Valencia region, Spain, *CATENA*, 45(3), 229–249, doi:10.1016/S0341-8162(01)00146-1, 2001.
- Camenen, B., Jodeau, M. and Jaballah, M.: Estimate of fine sediment deposit dynamics over a gravel bar using photography analysis Estimate of fine sediment deposit dynamics on a gravel bar using photography analysis, *Int. J. Sediment Res.*, 28(2), doi:10.1016/S1001-6279(13)60033-5i, 2013.
- Carbonneau, P. E., Bergeron, N. E. and Lane, S. N.: Texture-based image segmentation applied to the quantification of superficial sand in salmonid river gravels, *Earth Surf. Process. Landforms*, 30(1), 121–127, doi:10.1002/esp.1140, 2005.
- Chow, T. C., Maidment, D.R., Mays, L. W.: *Applied Hydrology*, McGraw Hill Series in Water Resources and Environmental Engineering., 1988.
- Cole, S. J. and Moore, R. J.: Hydrological modelling using raingauge- and radar-based estimators of areal rainfall, *J. Hydrol.*, 358(3–4), 159–181, doi:10.1016/J.JHYDROL.2008.05.025, 2008.
- Costabile, P. and Macchione, F.: Enhancing river model set-up for 2-D dynamic flood modelling, *Environ. Model. Softw.*, 67, 89–107, doi:10.1016/j.envsoft.2015.01.009, 2015.
- Curebal, I., Efe, R., Ozdemir, H., Soykan, A. and Sönmez, S.: GIS-based approach for flood analysis: case study of Keçidere flash flood event (Turkey), *Geocarto Int.*, 31(4), 355–366, doi:10.1080/10106049.2015.1047411, 2016.
- Delrieu, G., Nicol, J., Yates, E., Kirstetter, P.-E., Creutin, J.-D., Anquetin, S., Obled, C., Saulnier, G.-M., Ducrocq, V., Gaume, E., Payrastre, O., Andrieu, H., Aral, P.-A., Bouvier, C., Neppel, L., Livet, M., Lang, M., du-Châtelet, J. P., Walpersdorf, A., Wobrock, W., Delrieu, G., Nicol, J., Yates, E., Kirstetter, P.-E., Creutin, J.-D., Anquetin, S., Obled, C., Saulnier, G.-M., Ducrocq, V., Gaume, E., Payrastre, O., Andrieu, H., Aral, P.-A., Bouvier, C., Neppel, L., Livet, M., Lang, M., du-Châtelet, J. P., Walpersdorf, A. and Wobrock, W.: The Catastrophic Flash-Flood Event of 8–9 September 2002 in the Gard Region, France: A First Case Study for the Cévennes–Vivarais Mediterranean Hydrometeorological Observatory, *J. Hydrometeorol.*, 6(1), 34–52, doi:10.1175/JHM-400.1, 2005.



- 615 DGRHH: Estudio de caracterización del régimen extremo de precipitaciones en la isla de mallorca, Madrid., 2001.  
Doswell, C. A., Ramis, C., Romero, R. and Alonso, S.: A Diagnostic Study of Three Heavy Precipitation Episodes in the  
Western Mediterranean Region, *Weather Forecast.*, 13(1), 102–124, doi:10.1175/1520-  
0434(1998)013<0102:ADSOTH>2.0.CO;2, 1998.
- 620 European Environment Agency: Flood risks and environmental vulnerability exploring the synergies between floodplain  
restoration, water policies and thematic policies, Publications Office of the European Union., 2016.  
Gaume, E., Bain, V., Bernardara, P., Newinger, O., Barbuc, M., Bateman, A., Blaškovičová, L., Blöschl, G., Borga, M.,  
Dumitrescu, A., Daliakopoulos, I., Garcia, J., Irimescu, A., Kohnova, S., Koutroulis, A., Marchi, L., Matreata, S., Medina, V.,  
Preciso, E., Sempere-Torres, D., Stancalie, G., Szolgay, J., Tsanis, I., Velasco, D. and Viglione, A.: A compilation of data on  
European flash floods, *J. Hydrol.*, 367(1–2), 70–78, doi:10.1016/J.JHYDROL.2008.12.028, 2009.
- 625 Grimalt, M. and Rodríguez-Perea, A.: Cabals màxims al Llevant i Migjorn de Mallorca durant les revingudes del setembre de  
1989, *Treballs Geogr.*, 42, 7–18, 1989.  
Hamill, T. M., Whitaker, J. S., Hamill, T. M. and Whitaker, J. S.: Probabilistic Quantitative Precipitation Forecasts Based on  
Reforecast Analogs: Theory and Application, *Mon. Weather Rev.*, 134(11), 3209–3229, doi:10.1175/MWR3237.1, 2006.  
Horritt, M. S. and Bates, P. D.: Evaluation of 1D and 2D numerical models for predicting river flood inundation, *J. Hydrol.*,  
630 268(1–4), 87–99, doi:10.1016/S0022-1694(02)00121-X, 2002.  
Hunter, S. M.: WSR-88D RADAR RAINFALL ESTIMATION: CAPABILITIES, LIMITATIONS AND POTENTIAL  
IMPROVEMENTS, *Natl. Weather Dig.*, 20(4), 26–38, 1996.  
IPCC: Managing the Risks of Extreme Events and Disasters to Advance Climate Change Adaptation., 2012.
- 635 Jankov, I., Berner, J., Beck, J., Jiang, H., Olson, J. B., Grell, G., Smirnova, T. G., Benjamin, S. G., Brown, J. M., Jankov, I.,  
Berner, J., Beck, J., Jiang, H., Olson, J. B., Grell, G., Smirnova, T. G., Benjamin, S. G. and Brown, J. M.: A Performance  
Comparison between Multiphysics and Stochastic Approaches within a North American RAP Ensemble, *Mon. Weather Rev.*,  
145(4), 1161–1179, doi:10.1175/MWR-D-16-0160.1, 2017.  
Khattak, M. S., Anwar, F., Saeed, T. U., Sharif, M., Sheraz, K. and Ahmed, A.: Floodplain Mapping Using HEC-RAS and  
ArcGIS: A Case Study of Kabul River, *Arab. J. Sci. Eng.*, 41(4), 1375–1390, doi:10.1007/s13369-015-1915-3, 2016.
- 640 Knebl, M. R., Yang, Z.-L., Hutchison, K. and Maidment, D. R.: Regional scale flood modeling using NEXRAD rainfall, GIS,  
and HEC-HMS/RAS: a case study for the San Antonio River Basin Summer 2002 storm event, *J. Environ. Manage.*, 75(4),  
325–336, doi:10.1016/J.JENVMAN.2004.11.024, 2005.  
Kolios, S. and Feidas, H.: A warm season climatology of mesoscale convective systems in the Mediterranean basin using  
satellite data, *Theor. Appl. Climatol.*, 102(1–2), 29–42, doi:10.1007/s00704-009-0241-7, 2010.
- 645 Lillesand, T. M., Kiefer, R. W. and Chipman, J. W.: Remote sensing and image interpretation., 2015.  
Llasat, M. C., Llasat-Botija, M., Prat, M. A., PorcúPorc, F., Price, C., Mugnai, A., Lagouvardos, K., Kotroni, V., Katsanos,  
D., Michaelides, S., Yair, Y., Savvidou, K. and Nicolaidis, K.: High-impact floods and flash floods in Mediterranean countries:  
the FLASH preliminary database., 2010.  
Llasat, M. C., Marcos, R., Llasat-Botija, M., Gilabert, J., Turco, M. and Quintana-Seguí, P.: Flash flood evolution in North-  
650 Western Mediterranean, *Atmos. Res.*, 149, 230–243, doi:10.1016/J.ATMOSRES.2014.05.024, 2014.  
MAPAMA: Sistema Nacional de Cartografía de Zonas Inundables., 2010.  
Marchi, L., Borga, M., Preciso, E. and Gaume, E.: Characterisation of selected extreme flash floods in Europe and implications  
for flood risk management, *J. Hydrol.*, 394(1–2), 118–133, doi:10.1016/J.JHYDROL.2010.07.017, 2010.  
Marchi, L., Cavalli, M., Amponsah, W., Borga, M. and Crema, S.: Upper limits of flash flood stream power in Europe,  
655 *Geomorphology*, 272, 68–77, doi:10.1016/J.GEOMORPH.2015.11.005, 2016.  
Merritt, D. M. and Wohl, E. E.: Downstream hydraulic geometry and channel adjustment during a flood along an ephemeral,  
arid-region drainage, *Geomorphology*, 52(3–4), 165–180, doi:10.1016/S0169-555X(02)00241-6, 2003.  
Montaldo, N., Toninelli, V., Albertson, J. D., Mancini, M. and Troch, P. A.: The effect of background hydrometeorological  
conditions on the sensitivity of evapotranspiration to model parameters: analysis with measurements from an Italian alpine  
660 catchment, *Hydrol. Earth Syst. Sci.*, 7(6), 848–861, doi:10.5194/hess-7-848-2003, 2003.  
Nguyen, H. Q., Degener, J. and Kappas, M.: Flash Flood Prediction by Coupling KINEROS2 and HEC-RAS Models for  
Tropical Regions of Northern Vietnam, , 242–265, doi:10.3390/hydrology2040242, 2015.  
Nuissier, O., Joly, B., Joly, A., Ducrocq, V. and Arbogast, P.: A statistical downscaling to identify the large-scale circulation  
patterns associated with heavy precipitation events over southern France, *Q. J. R. Meteorol. Soc.*, 137(660), 1812–1827,



- 665 doi:10.1002/qj.866, 2011.  
Ortega, J. A. and Garzón-Heydt, G.: Geomorphological and sedimentological analysis of flash-flood deposits: The case of the 1997 Rivillas flood (Spain), *Geomorphology*, 112(1–2), 1–14, doi:10.1016/J.GEOMORPH.2009.05.004, 2009.
- Papaioannou, G., Loukas, A., Vasiliades, L. and Aronica, G. T.: Flood inundation mapping sensitivity to riverine spatial resolution and modelling approach, *Nat. Hazards*, 83(1), 117–132, doi:10.1007/s11069-016-2382-1, 2016.
- 670 Papaioannou, G., Efstratiadis, A., Vasiliades, L., Loukas, A., Papalexioiu, S., Koukouvinos, A., Tsoukalas, I. and Kossieris, P.: An Operational Method for Flood Directive Implementation in Ungauged Urban Areas, *Hydrology*, 5(2), 24, doi:10.3390/hydrology5020024, 2018.
- Pellarin, T., Delrieu, G., Saulnier, G.-M., Andrieu, H., Vignal, B., Creutin, J.-D., Pellarin, T., Delrieu, G., Saulnier, G.-M., Andrieu, H., Vignal, B. and Creutin, J.-D.: Hydrologic Visibility of Weather Radar Systems Operating in Mountainous  
675 Regions: Case Study for the Ardèche Catchment (France), *J. Hydrometeorol.*, 3(5), 539–555, doi:10.1175/1525-7541(2002)003<0539:HVOWRS>2.0.CO;2, 2002.
- Rabuffetti, D., Ravazzani, G., Corbari, C. and Mancini, M.: Verification of operational Quantitative Discharge Forecast (QDF) for a regional warning system &ndash; the AMPHORE case studies in the upper Po River, *Nat. Hazards Earth Syst. Sci.*, 8(1), 161–173, doi:10.5194/nhess-8-161-2008, 2008.
- 680 Ravazzani, G., Corbari, C., Morella, S., Gianoli, P. and Mancini, M.: Modified Hargreaves-Samani Equation for the Assessment of Reference Evapotranspiration in Alpine River Basins, *J. Irrig. Drain. Eng.*, 138(7), 592–599, doi:10.1061/(ASCE)IR.1943-4774.0000453, 2012.
- Ravazzani, G., Amengual, A., Ceppi, A., Homar, V., Romero, R., Lombardi, G. and Mancini, M.: Potentialities of ensemble strategies for flood forecasting over the Milano urban area, *J. Hydrol.*, 539, 237–253, doi:10.1016/J.JHYDROL.2016.05.023,  
685 2016.
- Righini, M., Surian, N., Wohl, E., Marchi, L., Comiti, F., Amponsah, W. and Borga, M.: Geomorphic response to an extreme flood in two Mediterranean rivers (northeastern Sardinia, Italy): Analysis of controlling factors, *Geomorphology*, 290, 184–199, doi:10.1016/J.GEOMORPH.2017.04.014, 2017.
- Romero, R., Sumner, G., Ramis, C. and Genovés, A.: A classification of the atmospheric circulation patterns producing significant daily rainfall in the Spanish Mediterranean area, *Int. J. Climatol.*, 19(7), 765–785, doi:10.1002/(SICI)1097-0088(19990615)19:7<765::AID-JOC388>3.0.CO;2-T, 1999.
- Ruiz-Villanueva, V., Bodoque, J. M., Díez-Herrero, A., Eguibar, M. A. and Pardo-Igúzquiza, E.: Reconstruction of a flash flood with large wood transport and its influence on hazard patterns in an ungauged mountain basin, *Hydrol. Process.*, 27(24), 3424–3437, doi:10.1002/hyp.9433, 2013.
- 695 Ruiz Villanueva, V., Bladé Castellet, E., Díez-Herrero, A., Bodoque, J. M. and Sánchez-Juny, M.: Two-dimensional modelling of large wood transport during flash floods, *Earth Surf. Process. Landforms*, 39(4), 438–449, doi:10.1002/esp.3456, 2014.
- Sabat, F., Muñoz, J. A. and Santanach, P.: Transversal and oblique structures at the Serres de Llevant thrust belt (Mallorca Island), *Geol. Rundschau*, 77(2), 529–538, doi:10.1007/BF01832396, 1988.
- Schumann, G. J., Muhlhausen, J. and Andreadis, K. M.: Rapid Mapping of Small-Scale River-Floodplain Environments Using UAV SfM Supports Classical Theory, , 1–12, doi:10.3390/rs11080982, 2019.
- 700 Tarolli, P., Borga, M., Morin, E., Delrieu, G. and Delrieu Analysis, G.: Analysis of flash flood regimes in the North-Western and South-Eastern Mediterranean regions, *Eur. Geosci. Union*, 12, 1255–1265, doi:10.5194/nhess-12-1255-2012i, 2012.
- Teng, J., Jakeman, A. J., Vaze, J., Croke, B. F. W., Dutta, D. and Kim, S.: Flood inundation modelling: A review of methods, recent advances and uncertainty analysis, *Environ. Model. Softw.*, 90, 201–216, doi:10.1016/J.ENVSOFT.2017.01.006, 2017.
- 705 US Army Corps of Engineers: HEC-RAS River Analysis System Hydraulic Reference Manual, Version 5., Davis (California), 2016.
- USDA: Urban Hydrology for Small Watersheds, USDA TR-55., 1986.
- Wilks, D. S.: Use of stochastic weathergenerators for precipitation downscaling, *Wiley Interdiscip. Rev. Clim. Chang.*, 1(6), 898–907, doi:10.1002/wcc.85, 2010.
- 710 Yalcin, E.: Two-dimensional hydrodynamic modelling for urban flood risk assessment using unmanned aerial vehicle imagery: A case study of Kirsehir, Turkey, *J. Flood Risk Manag.*, (April), 1–14, doi:10.1111/jfr3.12499, 2018.
- Yochum, S. E., Sholtes, J. S., Scott, J. A. and Bledsoe, B. P.: Stream power framework for predicting geomorphic change: The 2013 Colorado Front Range flood, *Geomorphology*, 292, 178–192, doi:10.1016/J.GEOMORPH.2017.03.004, 2017.



Catchment	Area (km <sup>2</sup> )	Total rainfall (mm)	CN (II)	S <sub>0</sub> (mm)	λ	V <sub>hs</sub> (ms <sup>-1</sup> )	V <sub>cmax</sub> (ms <sup>-1</sup> )
Sant Llorenç	23.2	316.7	63.4 (10.0)	457.2	0.4	0.36	3.3

715

**Table 1** Calibrated parameters according to FEST-WB. Total rainfall amount and curve numbers are expressed as area-averaged values. Curve number standard deviation is shown between brackets. Note that curve numbers correspond to normal antecedent conditions and channel velocities to the maximum simulated celerities.

720

Land cover	Manning's n
Broad-leaved forest	0.1
Complex cultivation patterns	0.04
Coniferous forest	0.1
Discontinuous urban fabric	0.013
Fruit trees	0.08
Land principally occupied by agriculture	0.05
Mixed forest	0.1
Non-irrigated arable land	0.05
Sclerophyllous vegetation	0.05
Transitional Woodland-shrub	0.06

**Table 2** Manning's n roughness coefficient values used for flood modelling (adapted for CORINE land cover categories; Papaioannous et al., 2018).

725

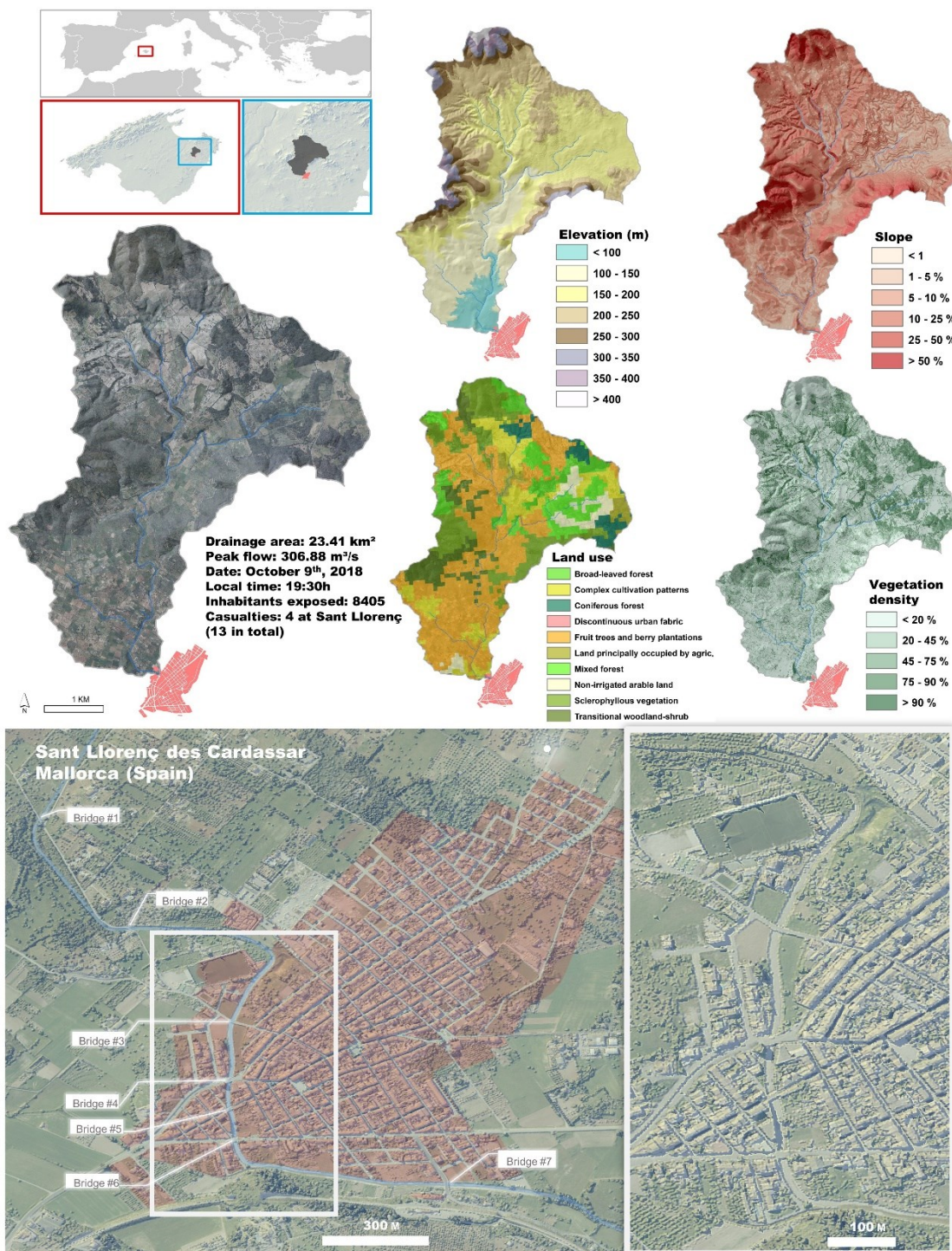


**Figure 1.** Study area location and overview. Upper panels: characteristics of the contributing watershed at Sant Llorenç (elevation, slope, land cover and LIDAR-derived vegetation density). Lower panels: detailed views of the urban interphase of the torrent de ses Planes at Sant Llorenç des Cardassar.

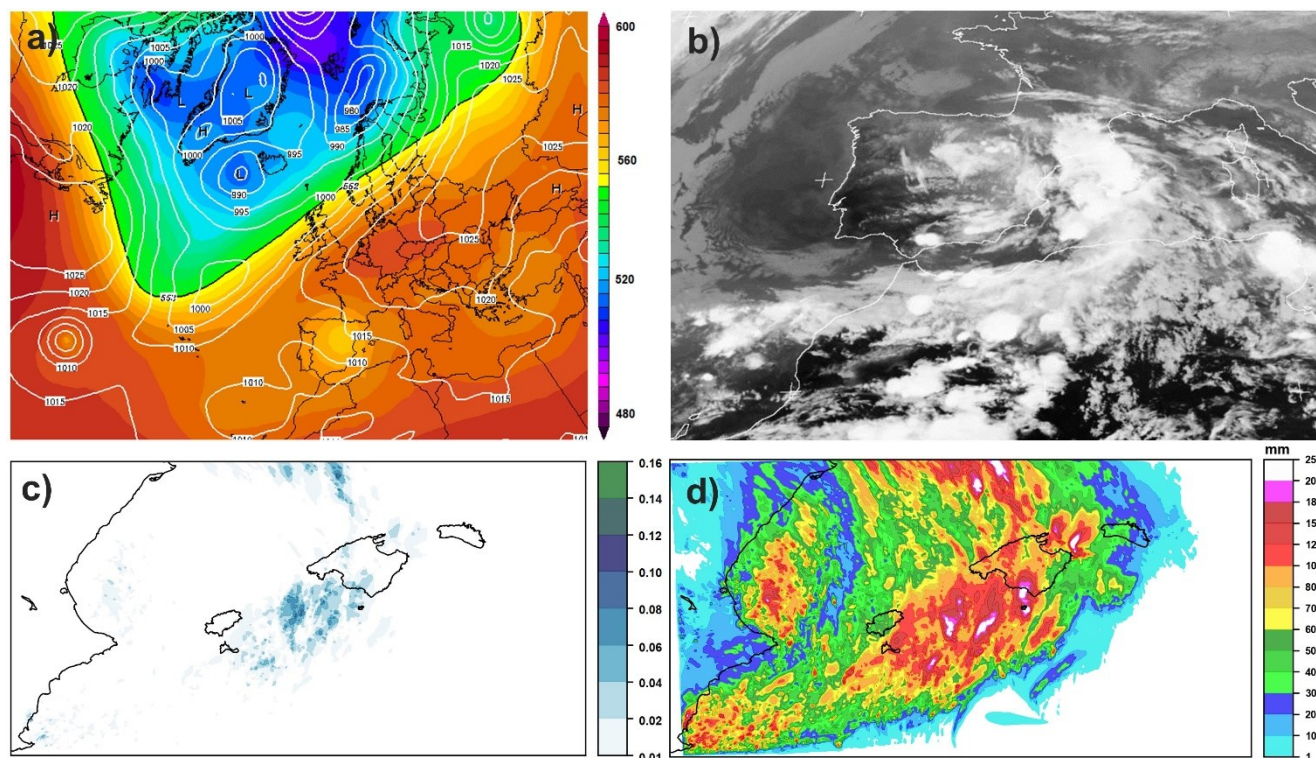
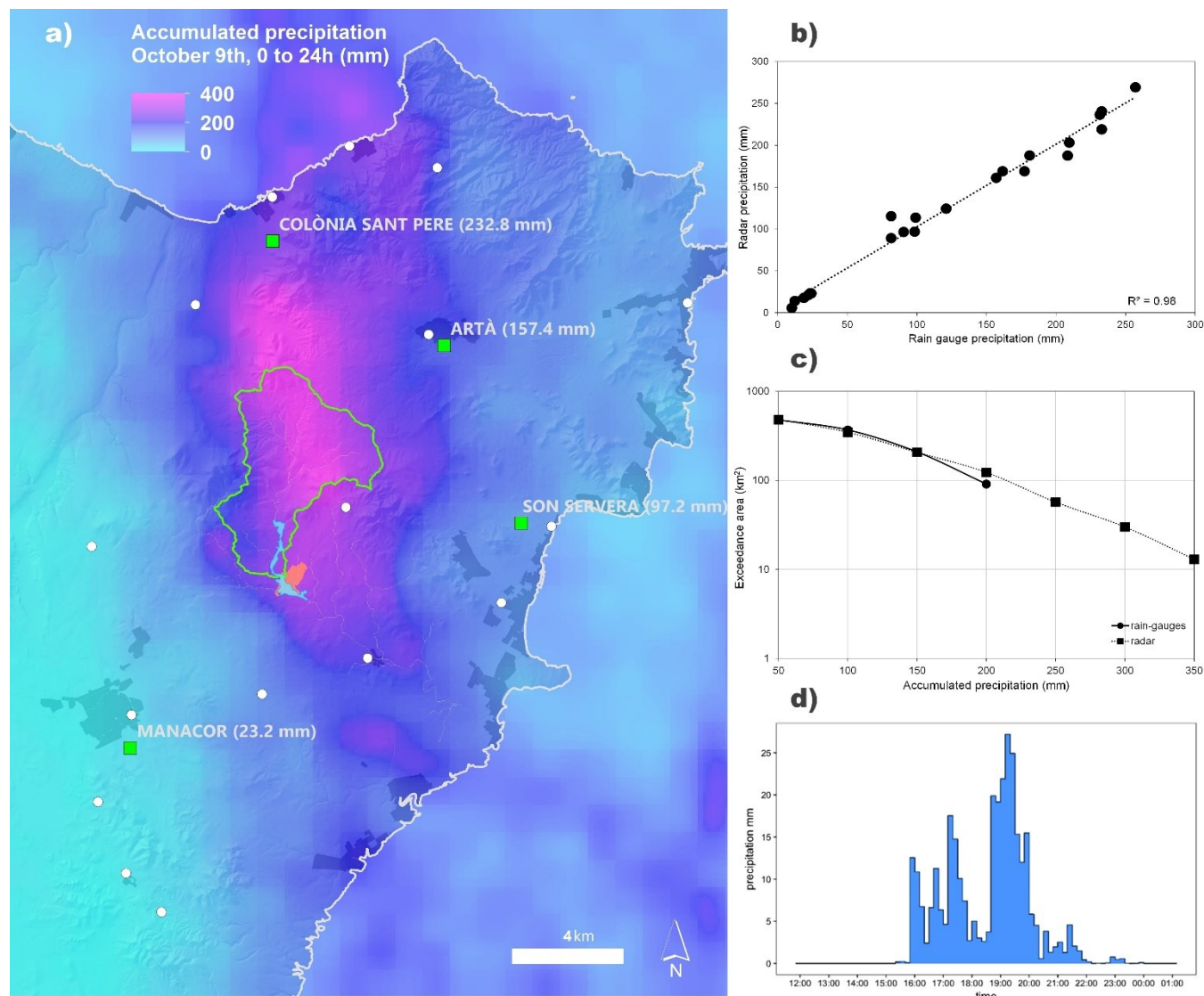


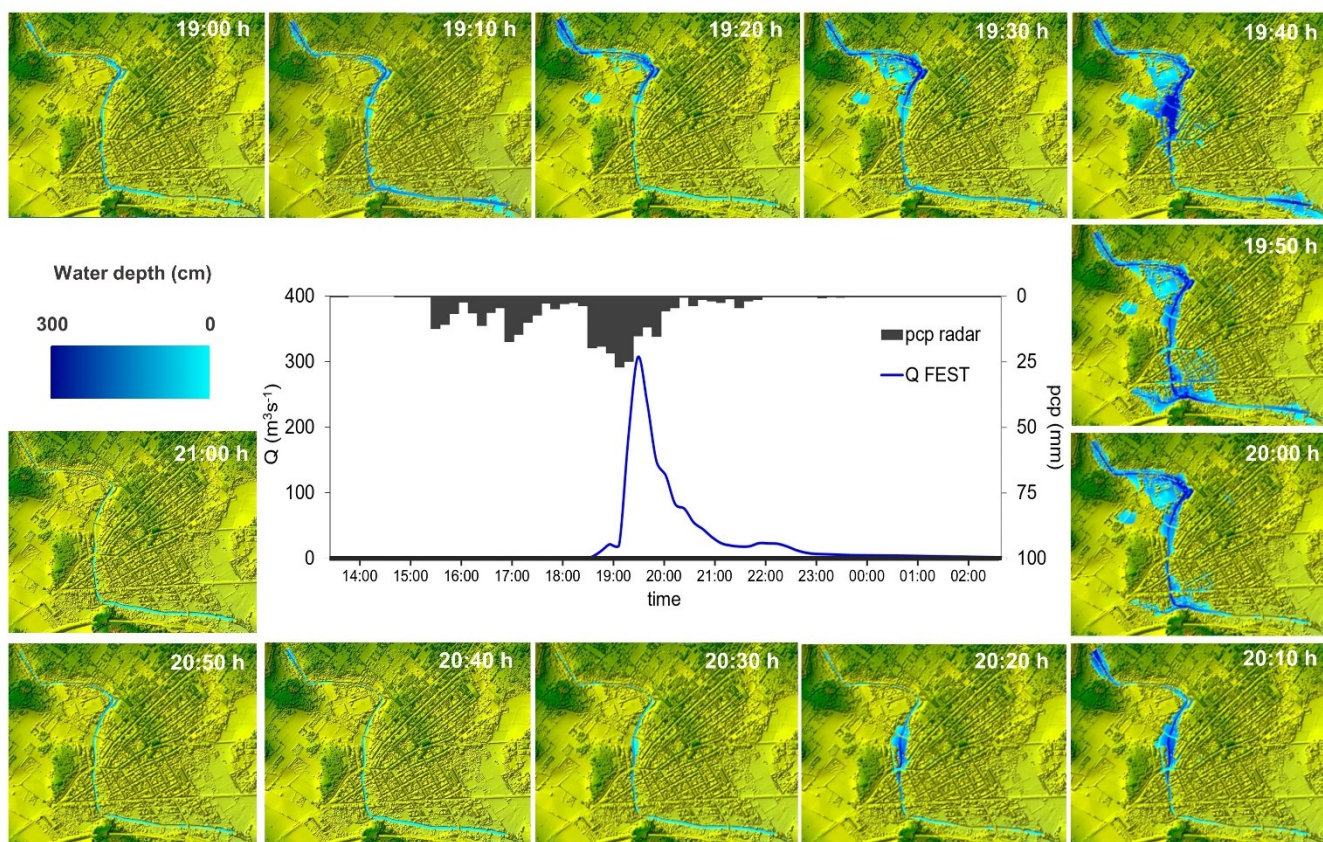
**Figure 2.** (a) Synoptic situation on October 9, 2018 at 12 UTC (1400h local time) from CFS reanalysis. Colors show geopotential height at 500 hPa (in gdam according to scale). White contours are isobars (hPa) at sea level (source: <https://www.wetterzentrale.de>; CC BY-NC). (b) IR MSG image corresponding to October 9, 2018 at 1700 UTC. (c) Probability of 12h-accumulated precipitation exceeding 100 mm valid at 00 UTC October 10, 2018 from the larger WRF domain initialized at 00 UTC October 9. (d) Maximum 12h-accumulated precipitation across ensemble members valid at 00 UTC October 10, 2018 from the larger WRF domain initialized at 00 UTC October 9.



740

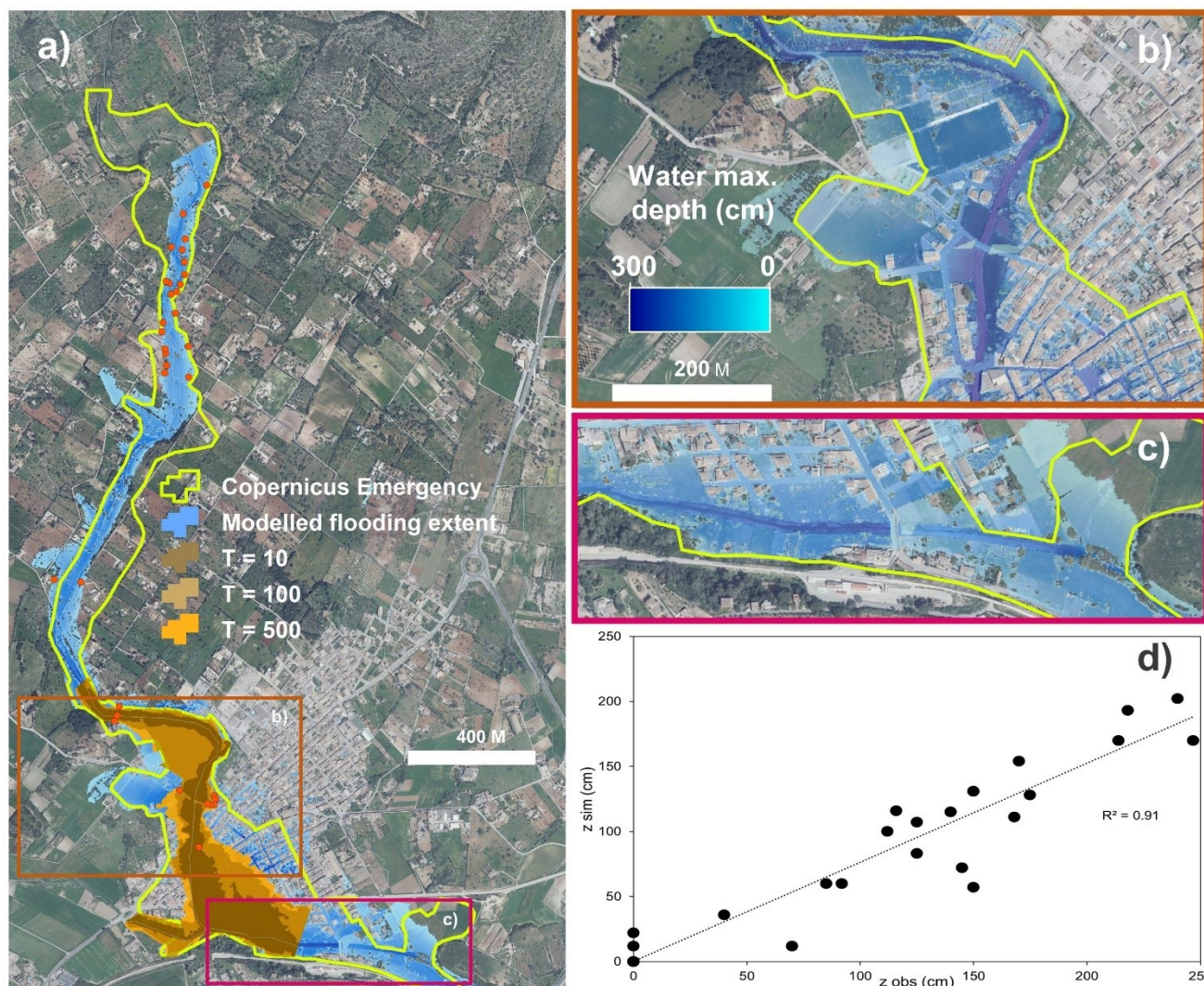
745

**Figure 3.** (a) Spatial distribution of the 24-h accumulated radar-estimated precipitation for the October 9, 2018 flashflood. Automatic raingauges used for bias correction are shown as squares. Circles depict the daily pluviometric stations. (b) scatterplot of the 24-h accumulated precipitation derived from radar estimates and pluviometric stations. (c) Comparison of the curves of exceedance areas for different rainfall thresholds derived from the 24-h accumulated pluviometric and radar-based rainfall amounts. All pluviometers shown in Fig. 3a have been used for the computation (21 stations). (d) Radar-driven precipitation for the October 9, 2018 episode at Sant Llorenç catchment.

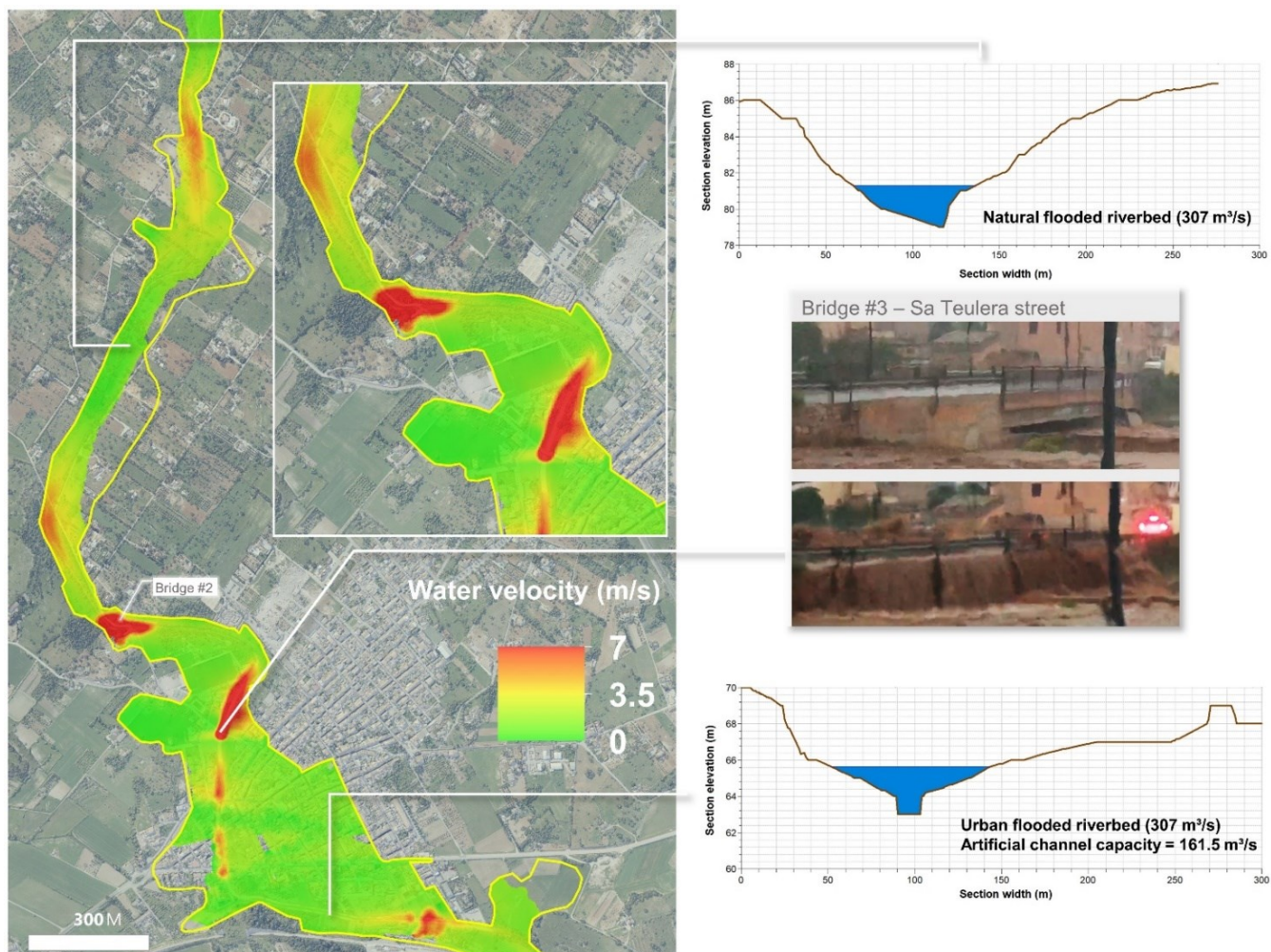


750

**Figure 4.** Modelled flash flood hydrograph at the entrance of Sant Llorenç and simulation of the flood peak as it crosses, devastating the town centre between 1900 h. and 2100 h.

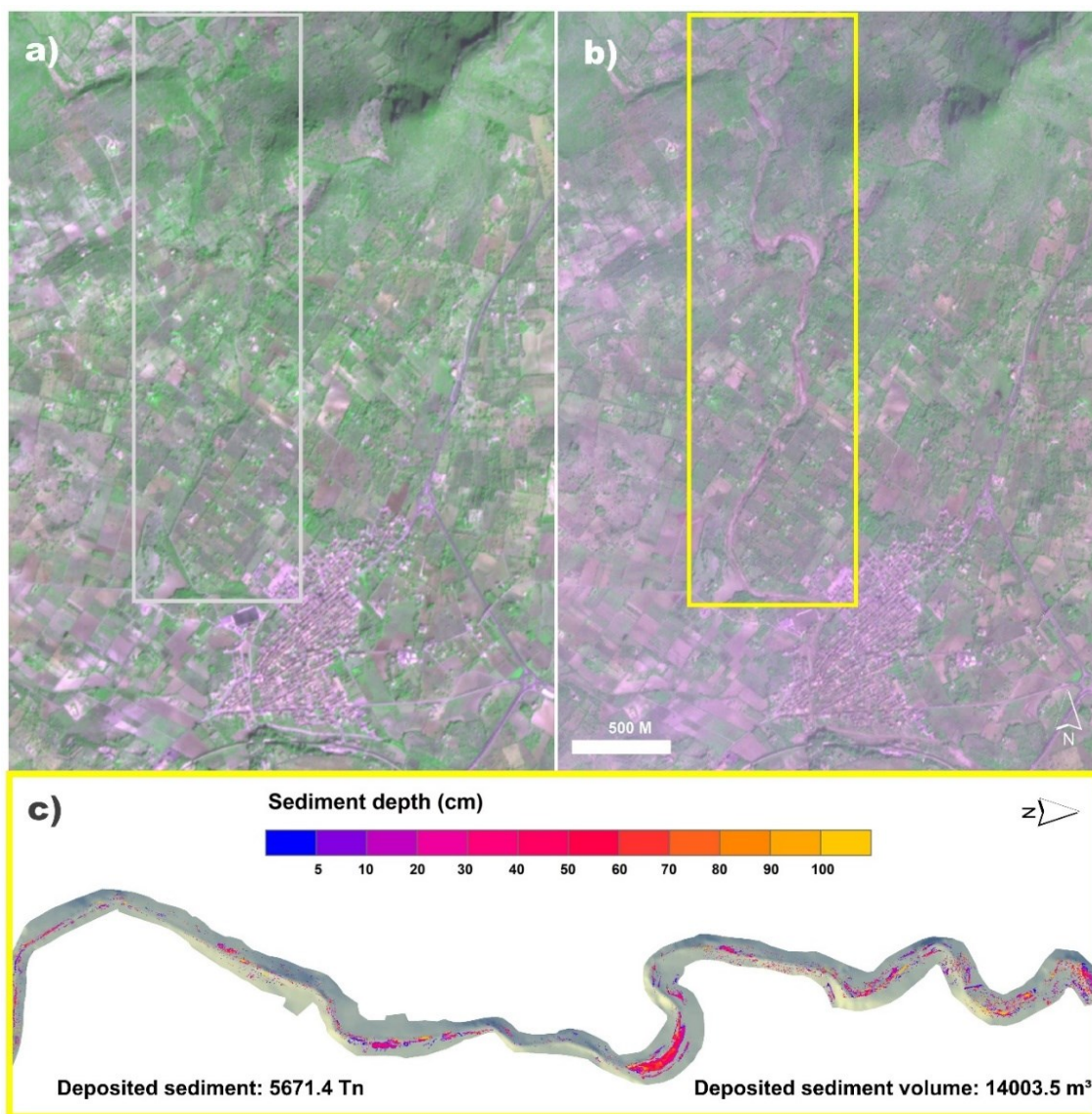


755 **Figure 5.** (a) Simulated flooding extent on the village (blue) compared with the observed event by Copernicus Emergency Management System (yellow contour) and selected return periods ( $T=10$ ,  $T=100$ ,  $T=500$ ); dots depict the flooding marks taken as reference to validate the simulation. Detailed views of modelled maximum water depths at Sant Llorenç town (b and c). Scatter plot showing the relationship between simulated water depths and in-situ measured flooding marks (d).



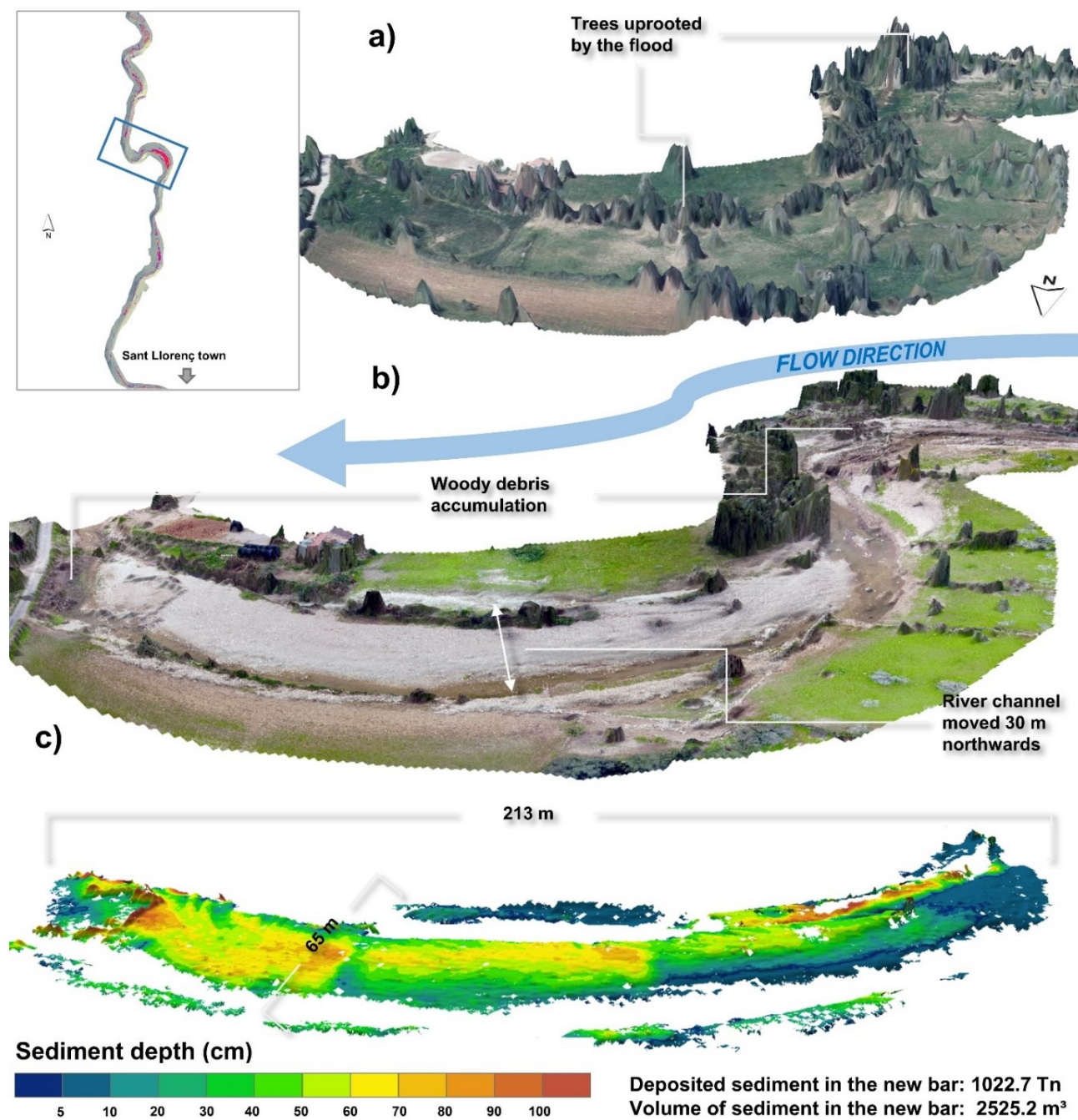
760

**Figure 6.** Left panel: simulated maximum water velocity across Sant Llorenç town during the event. Yellow contour line depicts the observed event by Copernicus Emergency Management System. Right panel: maximum discharge flowing through two sections, calculated from flooding marks and LIDAR point clouds, including velocities on the artificial concrete channel.



765

**Figure 7.** Effects of the catastrophic flash flood on the agricultural surroundings of Sant Llorenç town: sharpened false infrared RGB composites before, on October 9 (a), and after the event, on October 11 (b), derived from Planet® high resolution (3 m) imagery; (c) pixel histograms for selected land covers (herbaceous vegetation, shrubs and trees, water) and sediment types (coarse, mixed and fine) in the SfM-derived orthophotograph; (d) spatial patterns of sediment deposition and accumulation.



770

**Figure 8.** View of the Ses Planes stream at meander 2 km upstream of Sant Llorenç town: December 2014 orthophotograph (25 cm) superimposed onto a LIDAR-derived DEM (1m) before the event (a), and November 2018 orthophotograph (3 cm) dropped onto an SfM-derived DEM (6 cm) after the flash flood (b). Geomorphological changes and details of the sediment bar created during the flash flood at the meander (c).